

1 **Monitoring Salt Domes Used for Energy Storage with Microseismicity: Insights for a**
2 **Carbon-Neutral Future**

3
4
5 **Joses. Omojola¹, and Patricia Persaud¹**

6 ¹Department of Geosciences, University of Arizona.

7 Corresponding author: Joses Omojola (jomojo1@arizona.edu)

8
9 **Key Points:**

- 10 • Passive seismic monitoring with surface arrays is a non-invasive approach for identifying
11 subsurface hazards in salt domes.
- 12 • Clustered microearthquakes detected with our finetuned machine learning model
13 illuminate shear zone geometries and structural hazards.
- 14 • Cavern storage wells drilled within proximity of shear zones are at risk of safety
15 incidents.

16 Abstract

17 Underground storage in geologic formations will play a key role in the energy transition by
18 providing low-cost storage of renewable fuels like hydrogen. The sealing qualities of caverns
19 leached in salt and availability of domal salt bodies make them ideal for energy storage.
20 However, unstable boundary shear zones of anomalous friable salt can enhance internal shearing
21 and pose a structural hazard to storage operations. Considering the indistinct nature of internal
22 salt heterogeneities when imaged with conventional techniques like reflection seismic surveys,
23 we develop a method to map shear zones using seismicity patterns in the US Gulf Coast, the
24 region with the world's largest underground crude oil emergency supply. We developed and
25 finetuned a machine learning algorithm using tectonic and local microearthquakes. The finetuned
26 model was applied to detect microearthquakes in a 12-month nodal seismic dataset from the
27 Sorrento salt dome. Clustered microearthquake locations reveal the three-dimensional geometry
28 of two anomalous salt shear zones and their orientations were determined using probabilistic
29 hypocenter imaging. The seismicity pattern, combined with borehole pressure measurements,
30 and sonar surveys show the spatio-temporal evolution of cavern shapes within the salt dome. We
31 describe how shear zone seismicity contributed to a cavern well failure and gas release incident
32 that occurred during monitoring. Our findings show that caverns placed close to shear zones are
33 more susceptible to structural damage. We propose a non-invasive technique for mapping
34 hazards related to internal salt dome deformation that can be employed in high-noise industrial
35 settings to characterize salt domes used for storage.

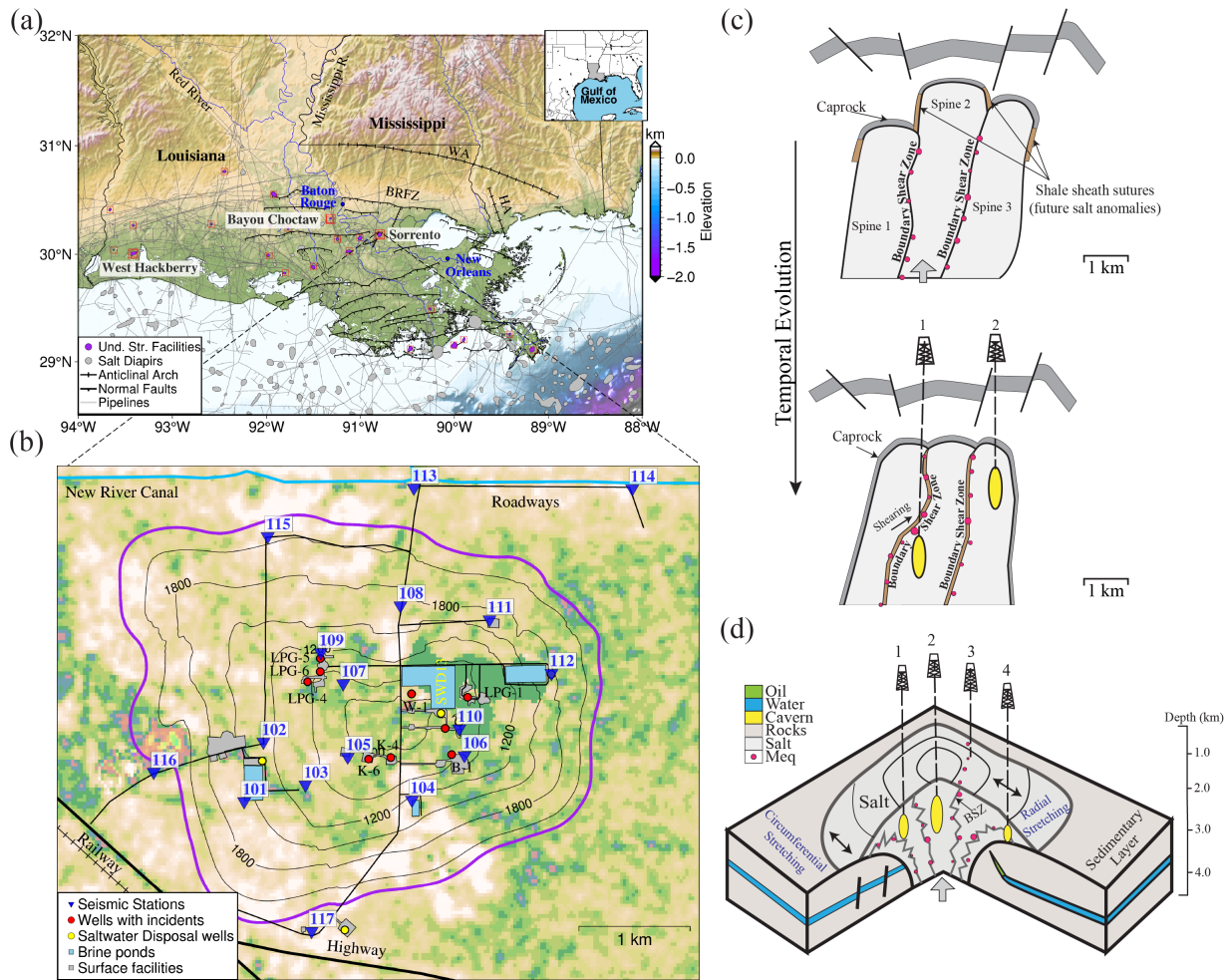
36 Plain Language Summary

37 In the shift towards renewable energy, underground storage is vital for increasing the feasibility
38 of fuels like hydrogen. Salt formations are ideal for storage, and caverns in salt domes are used
39 worldwide to store vast amounts of energy reserves. But salt domes can become unstable and
40 lead to cavern collapse, posing risks to the environment and nearby communities. Traditional
41 methods are expensive, often require drilled wells, and do not always spot hazards. We instead
42 used recordings of ground shaking from small earthquakes to identify them. By collecting these
43 recordings for over a year with an array of instruments installed at the surface over a Louisiana
44 salt dome, we were able to develop a new method for identifying very small earthquakes
45 allowing us to pinpoint hazardous areas. Our approach offers a non-invasive way for scientists
46 and engineers to assess hazards and mitigate risks associated with drilling and underground
47 storage operations in salt domes..

48 **1 Introduction**

49 The expansion of underground facilities capable of safely storing vast amounts of
50 renewable energy sources is a key component of the energy transition. Storage plays an
51 important role in balancing supply and demand by stockpiling excess energy and providing a
52 reliable backup during peak demand periods (Juez-Larré et al., 2019). Seasonal energy demands
53 have driven the need for underground storage facilities since 1915, e.g., over 20% of the natural
54 gas consumed in the United States each winter comes from underground storage facilities
55 (Beckman et al., 1995). Globally, over 148 sedimentary basins have salt formations suitable for
56 underground storage of fuels such as hydrogen, natural gas, and unrefined petroleum products.
57 However, most of the storage activity has been limited to technologically advanced countries in
58 Europe, Asia, and North America (Gillhaus & Horvath, 2008). In the United States,
59 underground storage is utilized in three major types of subsurface environments: depleted oil and
60 gas fields, aquifers, and salt caverns. The Gulf Coast states of Louisiana (**Figure 1a**) and Texas
61 have numerous salt domes (>90% of cavern fields in the US) and the largest facilities for state-
62 level gas storage in the country (Lord, 2009). They have the world's largest supply of emergency
63 crude oil, which is stored underground at four sites of the United States Strategic Petroleum
64 Reserves (SPR, 2022), and are well positioned to expand salt cavern capacity to meet increasing
65 energy demand.

66 Salt domes are extensively used for underground storage because of their favorable
67 geomechanical properties, large storage capacity, and low cushion gas requirements (Caglayan et
68 al., 2020). They are relatively safe, however, the presence of internal shear zones within these
69 salt structures can potentially compromise their stability and long-term functionality (Bérest et
70 al., 2019; Loeff, 2017). The non-optimal placement of caverns in salt domes has led to numerous
71 incidents that exceed the number of safety incidents recorded in oil and gas fields, and aquifers.
72 A study of safety incidents at underground storage facilities across the United States determined
73 that subsurface and well integrity problems contributed to 89% of recorded incidents in salt
74 caverns, compared to 44% in depleted oil and gas fields and 68% in aquifers (Evans & Schultz,
75 2017). Subsurface incidents in salt domes have been linked to caprock instability, overburden
76 faulting, and boundary shear zones (Evans, 2007; Loeff, 2017; Warren, 2017). Boundary shear
77 zones in salt domes are generally zones of impurities where surface water and hydrocarbons have
78 led to the formation of vugs, voids, or recrystallization of salt, making it weak and friable under
79 moderate conditions, or volatile and explosive under extreme conditions, where the rock salt has
80 been infused with gas (popping salt) (Davison, 2009; Jacoby, 1977; Warren, 2017). Laboratory
81 studies of normal Gulf Coast salt reveal that it is dominated by uniform grain sizes (~3-10 mm
82 diameter) of halite with banded layers or structureless features (Kupfer, 1990). Deviations from
83 this norm, such as high concentrations of anhydrite, potash salts, and impurities, can create
84 anomalous salt features (Davison, 2009; Loeff, 2017). Multiple anomalous features aligned
85 within a zone can form boundary shear zones (BSZs). Field studies of boundary shear zones
86 exposed within salt mines reveal that they can range in size from several meters to kilometers
87 and may traverse entire salt domes (Davison, 2009; Jackson et al., 2015; Jacoby, 1977) (**Figure**
88 **1d**). Unlike faults, BSZs can form through independent processes like hydrocarbon generation
89 within embedded shales that are not necessarily related to tectonic events. They often occur at
90 salt spine boundaries (see **Figure 1c**) due to differential upward movement of the spines. Using
91 current techniques, little to no information on shear zone emplacement is known at the onset of
92 underground storage projects, and wells are drilled using geomechanical models that are focused
93 on optimizing cavern design while overlooking shear zone hazards.



94

95 **Figure 1.** Overview of the Sorrento salt dome location and the evolution of boundary shear
 96 zones. (a) Regional map of salt domes in the US Gulf Coast, Louisiana and northern Gulf of
 97 Mexico. Domes used for underground storage are highlighted with red squares. The two US
 98 Strategic Petroleum Reserves and Sorrento domes are annotated. The map also shows regional
 99 structural features from Gillhaus and Horvath (2008) and gas pipelines with gray lines (EIA,
 100 2012). (b) Expanded map of the Sorrento salt dome showing the locations of the stations in the
 101 seismic array, and wells discussed in the text. Black contour lines indicate the top of the salt
 102 (Looff, 2017), and the outline of the dome is in purple. (c) Sketch depicting the development of
 103 shear zones in salt domes through time (Warren, 2017). Microearthquakes (meq) are shown with
 104 red circles. (d) 2.5D schematic representation of shear zone extent in a salt dome with overlying
 105 graben mimicking the Sorrento dome's geology.

106

107 The study of boundary shear zones (BSZ) in salt domes is crucial for various reasons.
 108 Firstly, accurate mapping and characterization of BSZs helps improve development strategies for
 109 early-stage underground storage projects by helping operators optimize cavern placement.
 110 Secondly, understanding the seismic behavior of shear zones is essential for assessing the risk of
 111 failure or leakage of wellbores in developed facilities, and early detection of casing or cavern
 112 collapse because placement near or within BSZs increases the potential for accidents due to
 113 reduced salt-structure quality (Jacoby, 1977). Accidents in salt domes highlight the critical

114 importance of studying subsurface hazards for both residents and the environment alike.
115 Between 1959 and 2012, over 26 incidents occurred at salt domes in the US (Ford & Dreger,
116 2020; Warren, 2017). Casing failures at salt domes have caused fires, resident evacuations, and
117 extensive damage to infrastructure and the environment amounting to millions of dollars (Evans,
118 2007). A cavern collapse along a disturbed rock zone at the Napoleonville salt dome in Bayou
119 Corne, Louisiana, in 2012 destroyed cypress trees within a 12-acre sinkhole, forced evacuations
120 of nearby residents due to gas leaks from collapsed caverns, and cost the operating company over
121 \$225 million in buyouts, remediation, and monitoring costs (Hanusik, 2019; Mitchell, 2018). In
122 1992, subsurface instability at the Weeks Island salt mine, Louisiana, resulted in the formation of
123 a 10-m wide sinkhole, requiring \$100 million for draining and remediation of existing caverns
124 (Bauer et al., 1997; Neal & Myers, 1994; Warren, 2017). They are also prone to outbursts, which
125 can be as large as the Belle Isle and Morton mine incidents that released over 220,000,000
126 standard cubic feet (scf) of gas and led to the loss of miners' lives (Ehgartner et al., 1998;
127 Plimpton et al., 1980; Warren, 2017).

128 To mitigate incidents in salt domes, shear zone mapping can be conducted using various
129 techniques. Sonar measurements and well logs have been utilized to identify boundary shear
130 zones (BSZs) in salt domes (Looff, 2017). 3D and 2D seismic surveys have been used to
131 characterize caprock geometric anomalies at domes and assess their potential seismic hazards
132 (Neal et al., 1993; Rautman et al., 2010). Foliation of halite crystals from cores have helped map
133 boundary shear zones that were not detected by reflection seismic surveys (Seni et al., 1984).
134 However, some of the shortcomings associated with mapping shear zones using the techniques
135 above are limited spatial samples from well data, and insufficient 3D seismic resolution within
136 salt deposits, which limits mapping of the shear zone outline to only along the overlying caprock
137 (Looff, 2017; Neal et al., 1993; Rautman et al., 2010). One way of constraining the location of
138 boundary shear zones is microearthquake monitoring. Passive seismic monitoring has been used
139 to detect seismic events such as rock falls, sliding motion, and fault movement within salt domes
140 (Ford & Dreger, 2020; Fortier et al., 2006). Although more affordable than borehole
141 installations, one challenge with surface seismic monitoring is the recordings of small magnitude
142 events can be masked by local equipment noise and anthropogenic sources which severely
143 inhibits event detection and location methods using travel-time techniques (Kinscher et al., 2015;
144 Mercerat et al., 2009). Post accident investigations of some safety incidents at salt domes have
145 detected seismicity prior to cavern collapse (Dreger & Ford, 2020; Mercerat et al., 2009),
146 however, the connection between shear zones and seismicity remains unclear.

147 Cavern operator reports of ground shaking at the Sorrento salt dome in Ascension Parish,
148 Louisiana, in January 2020 motivated us to install the SORRENTO array and investigate the
149 subsurface hazards and physical processes affecting drilled wells and excavated caverns. The
150 Sorrento salt dome is a slightly elongated salt diapir with an overlying graben system. The salt
151 body has a spatial extent of approximately 5 km by 4 km (Looff, 2017) ([Figure 1b](#)). It is located
152 in the Pontchartrain basin where over one third of Louisiana's population lives. Surface
153 conditions are swampy with an average elevation of 5 m above sea level. The area gets flooded
154 regularly following heavy rainfall and storms, sometimes restricting physical access to deploy
155 and retrieve seismometers. The dome is 40 km SE of the state capital, 70 km NW of New
156 Orleans, Louisiana and <19 km from the Maurepas swamp and wildlife management area
157 ([Figure 1a](#)). Salt layers are relatively shallow (1524 m depth), and oil and gas production occur
158 in flank traps to the north and south. The field has produced over 750 billion cubic feet (bcf) of
159 gas and 5000 million barrels of oil (mbo) (Petroleum, 2009), and saltwater is being disposed in

160 layers between 310 - 495 m depth on the eastern and western flanks of the dome (Consultants,
161 1990).

162 Currently, underground storage caverns within the Sorrento salt dome have a storage
163 capacity of 8.92 (bcf) of gas (SONRIS, 2022). Prior incidents resulted in the abandonment of two
164 early cavern wells (Looff, 2017) when anomalous salt features were encountered during drilling
165 and leaching. In May 2021, during monitoring, ground movement along a shear zone damaged
166 the LPG-5 cavern (**Figure 1b**), releasing 220,000 scf of nitrogen during a mechanical integrity
167 test, and creating a 6-9 m wide by 1.5 m deep crater on the ground surface beneath the wellhead
168 (LADNR, 2020a, 2021a).

169 In this study, we focus on monitoring seismic activity to identify zones of inferior salt
170 quality that can impact the integrity of well and cavern operations. We demonstrate with a 12-
171 month-long seismic dataset that seismicity can be linked to boundary shear zones at the Sorrento
172 dome, and analyze its connection to a recent storage cavern failure. We located clusters of
173 seismicity that can be used to identify unstable zones within salt, and extended mapping of
174 known shear zones away from well control. We believe this study can serve as an analog for how
175 storage caverns at other salt domes may be monitored to prevent future accidents, and highlight
176 the importance of understanding subsurface hazards as more cavern facilities are being
177 developed to meet rising energy storage needs.

178 **2 Data**

179 Our analysis was conducted using a combination of waveforms from nodal seismometers,
180 sonar surveys, and well data. The SORRENTO array was comprised of 17 stations installed
181 across the dome (**Figure 1b**) to record seismic data for 12 months. Each station was occupied
182 with a three-component SmartSolo 5 Hz nodal seismometers with self-contained GPS antenna
183 and battery that recorded at 500 Hz. Nodal seismometers were selected because of their ability to
184 be submerged underwater and deployed without the need for solar panels. We buried the nodes
185 in ~20-cm deep holes, covered with a couple of centimeters of soil to reduce the impact of noise
186 from the nearby highway, oilfield equipment, and frequent storms. The nodes were deployed in a
187 loosely circular grid depending on site accessibility to provide coverage around the flanks and
188 major cavern clusters near the center of the dome. Interstation distances varied between 0.2 - 1.9
189 km, and most sites were re-occupied during the 12 one-month installations that occurred between
190 February 2020 to July 2022 (**Table S1**).

191 Sonar surveys are acquired by cavern operators every 5 years in line with compliance
192 requirements dictated by the Louisiana Department of Natural Resources (LADNR), and we
193 digitized sonar surveys for caverns with available reports. Additionally, we analyzed the survey
194 reports and well data available at the LADNR SONRIS website (SONRIS, 2022). Event
195 information for regional and teleseismic earthquakes with magnitudes $>M_w$ 5 were obtained from
196 IRIS and the USGS to evaluate the possibility of external triggering of salt dome
197 microearthquakes.

198 **3 Methodology**

199 3.1 Event Detection and Phase Picking

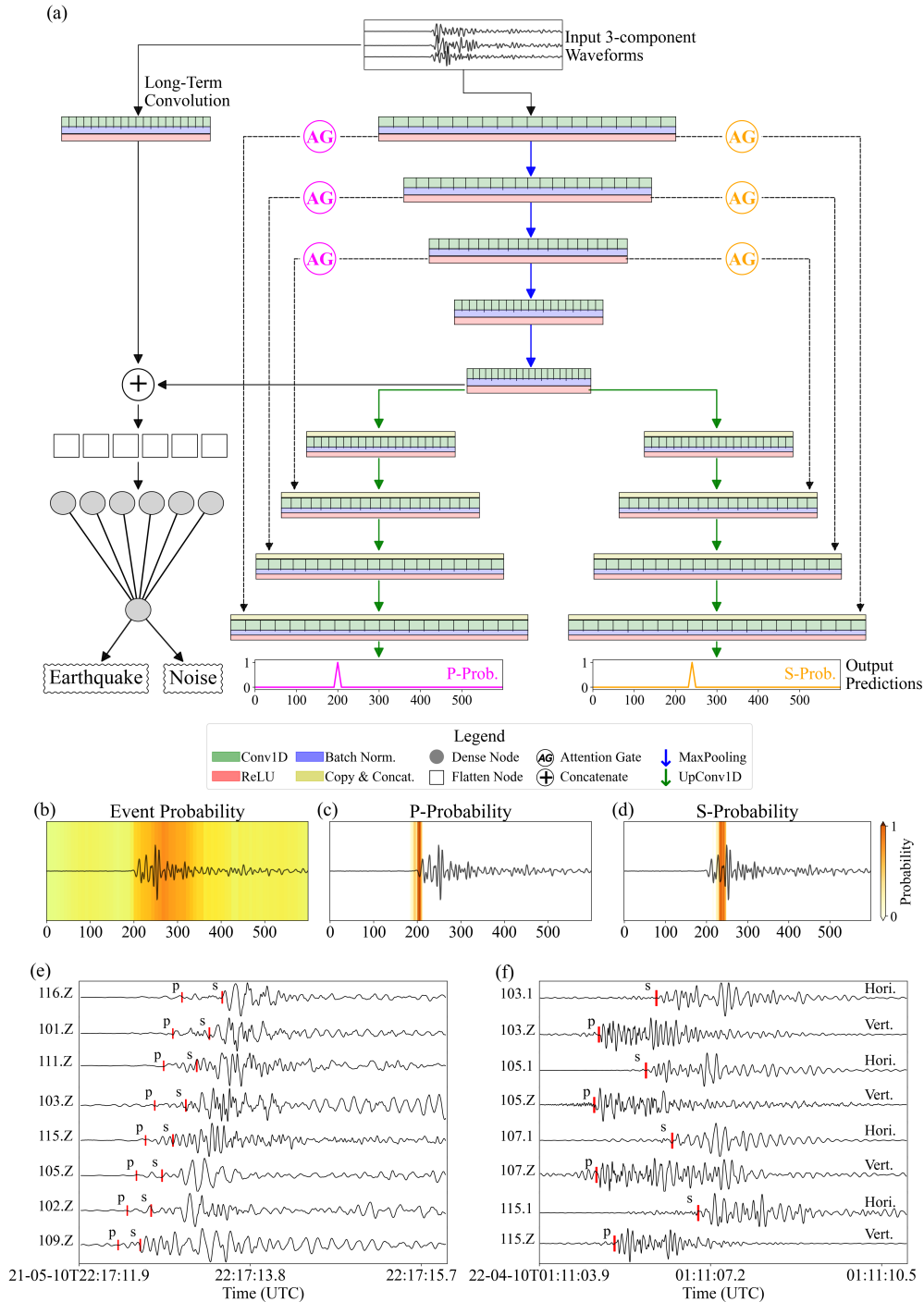
200 We initially employed the traditional short-term-average / long-term-average (STA/LTA)
201 methods for event detection with limited success. The STA/LTA technique resulted in a high
202 number of false positive detections originating from operating equipment around the dome. We
203 proceeded to test popular machine learning phase-pickers like EQTransformer, and PhaseNet
204 (Mousavi et al., 2020; Zhu & Beroza, 2019) for microearthquake detection. Adjusting the
205 parameters of the machine learning models reduced some of the false positive detections but
206 limited detection of many of the small microearthquakes (**Supplementary Text S2**). To achieve a
207 balance between microearthquake detection and minimizing false positives, we developed and
208 trained a hybrid U-Net model described below (**Figure 2a**) for event detection and phase picking
209 on salt dome microearthquakes. We trained the base hybrid U-Net model using a subset of the
210 Stanford Earthquake Dataset (STEAD) (Mousavi et al., 2019), and finetuned the model weights
211 using manually selected salt dome microearthquakes from the initial recordings at Sorrento. The
212 finetuned model predicts event detection probabilities and the position of body wave arrivals
213 simultaneously.

214 The finetuned model was applied to 6 s long sliding windows with a step size of 4 s
215 extracted from the Sorrento array. An event was recorded when a minimum of four adjacent
216 stations were triggered (detection probability from the hybrid U-Net > 95%, and phase
217 probabilities > 50%) within a 6 s time window. This served as a simple association method, and
218 thresholding the detections across both the array and at each individual station helped with
219 eliminating false positive detections or spikes that could be localized at individual stations.
220 Associated picks were manually quality checked to remove outlier detections, and improve the
221 quality of the event location process.

222 3.1.1 Waveform Preprocessing

223 Training data for the base model was obtained from subset of the Stanford Earthquake
224 Dataset (STEAD) (Mousavi et al., 2019). We filtered the STEAD catalog to select only events
225 with magnitudes $M_w < 3$ and epicentral distances < 5.5 km to mimic the expected seismic activity
226 at Sorrento (**Figure S4a**). The subset included (200 K) event and noise waveforms randomly
227 split into training, validation, and test sets (90%, 5%, 5%).

228 Raw waveforms in counts were downloaded from the nodes and the corresponding
229 instrument response file was obtained from the IRIS Nominal Response Library. We detrended
230 the waveforms and converted them to displacement amplitudes using standard procedures from
231 the ObsPy package (Krischer et al., 2017). We manually selected 500 salt dome event and noise
232 waveforms to finetune the model and downsampled the data to 100 Hz. The finetuning
233 waveform data were split in a similar manner to the base model waveforms. Binary labels were
234 used for event detection, and phase pick labels were generated by convolving a triangular
235 function with the onset time of the phase picks (**Figure 2a**).



236

237 **Figure 2.** The hybrid U-Net model for seismic event detection. (a) Architecture of the detection
 238 model showing input waveforms and output predictions. (b-d) Gradient class activation map
 239 (Grad-CAM) of the model's event, P-wave, and S-wave detection probability. Hot colors have
 240 higher probabilities. (e) Vertical displacement waveforms from the microearthquake recorded
 241 during the mechanical integrity test (MIT) at the LPG-5 cavern, showing impulsive P-wave
 242 arrivals. (f) Examples of vertical and horizontal waveforms from a microearthquake detected
 243 with the hybrid model showing P- and S-wave arrivals, respectively.

244 3.1.2 Model Training and Evaluation

245 We modify the Attention U-Net (Oktay et al., 2018; Ronneberger et al., 2015) for 1D
 246 convolution (Figure 2a). The input for the model consisted of 3-component waveforms cropped
 247 into 6-s long recordings and downsampled to 100 Hz. The training data was augmented by
 248 randomly shifting the event origin within the 6-s window. A single convolution layer with longer
 249 kernels was appended to the vanilla Attention U-Net to mimic the LTA and we refer to this layer
 250 as a long-term-average convolution (LTC) layer (Figure 2a). Using the LTC layer further
 251 stabilized the event detection weights during training and improved the validation loss (Figure
 252 S4b). The input waveforms were passed through four down-sampling convolution layers, and
 253 rectified linear unit (ReLU) activation, batch normalization and same padding were applied to
 254 each layer. We split the bottle-neck convolution output into three, where one of the outputs was
 255 concatenated with the LTC output and passed through a series of dense layers to produce a
 256 binary classification of either event or noise. The remaining two outputs from the bottle-neck
 257 layer were concatenated with skip connections from attention gates and upsampled to match the
 258 number of triangular label samples used for P- and S- arrivals (Figure 2a). We used the sigmoid
 259 activation function to set probabilities for the final layers of all the model outputs

$$260 \quad S(x) = \frac{1}{1 + e^{-x}} = \frac{e^x}{e^x + 1} = 1 - S(-x) \quad (1)$$

261 We used the binary cross-entropy loss function which computes the following average:

$$262 \quad Loss = -\frac{1}{output\ size} \sum_{i=1}^{output\ size} y_i \cdot \log \hat{y}_i + (1 - y_i) \cdot \log(1 - \hat{y}_i) \quad (2)$$

263 where \hat{y}_i is the i -th scalar in the model output, y_i is the corresponding target value, and the
 264 output size is the number of scalar values in the model output. The output from the phase picker
 265 model head is a probability distribution for all points in the input timeseries. We stopped training
 266 after the validation loss did not improve for 10 consecutive epochs. The diagnostic accuracy of
 267 the model measured with the Area under the Curve (AUC) for the Receiver Operating
 268 Characteristic (ROC) was 1 on the STEAD data, and 0.996 on the Sorrento events. Additional
 269 evaluation metrics used to assess model performance are described in [Supplementary Text S2](#).
 270 Grad-CAM maps show segments of a waveform that the finetuned model pays attention to for
 271 classifying events and picking phase arrivals (Figure 2b-d).

272 3.2 Event Location

273 The events were located using the HYPOINVERSE 1.40 software (Klein, 2002) with a
 274 1D velocity model (Table S2) because of ease of computation. Velocities for the shallow part of
 275 the 1D velocity model were obtained from the sonic logs of the Exxon SWD-13 well
 276 (Schlumberger, 2004), and a constant velocity of 4.0 km/s was used for the salt layers. A V_P/V_S
 277 ratio of 1.72 was selected based on previous salt dome studies (Kinscher et al., 2015; Nayak,
 278 2014). A minimum of 4 stations were required to locate an event and a starting trial depth of 500
 279 m was used in the event location workflow.

280 The HYPODD program (Waldhauser, 2001) was used to obtain the double-difference
 281 locations from the initial HYPOINVERSE catalog. The difference in absolute travel times from
 282 different events at the same station were optimized with the conjugate gradient method and

283 damping. The degree of damping was determined by adjusting the system to obtain a stable
 284 condition number (Waldhauser, 2001). Phases for events separated by a maximum distance of 5
 285 km were linked, and a minimum of four observations per event was required to obtain the final
 286 relocated event catalog. Monte Carlo simulations of best fit fault planes through the clustered
 287 relocated catalog were calculated using a hypocenter-based 3D imaging program (Truttmann et
 288 al., 2023). Additional details are provided in [Supplementary Text S3](#).

289 3.3 Event Magnitudes

290 We calculated the local earthquake magnitude (M_L) by removing the instrument response
 291 to obtain displacement waveforms. The seismograms were bandpass filtered between 0.1 and 50
 292 Hz and windowed 0.5 s before and 2 s after the P-arrival. The peak amplitude A_{max} is computed
 293 within this window and the local magnitude is expressed as follows:

$$294 \quad M_L = \log_{10}(2800 \cdot A_{max}) + 1.27 \cdot \log_{10} D + a \quad (3)$$

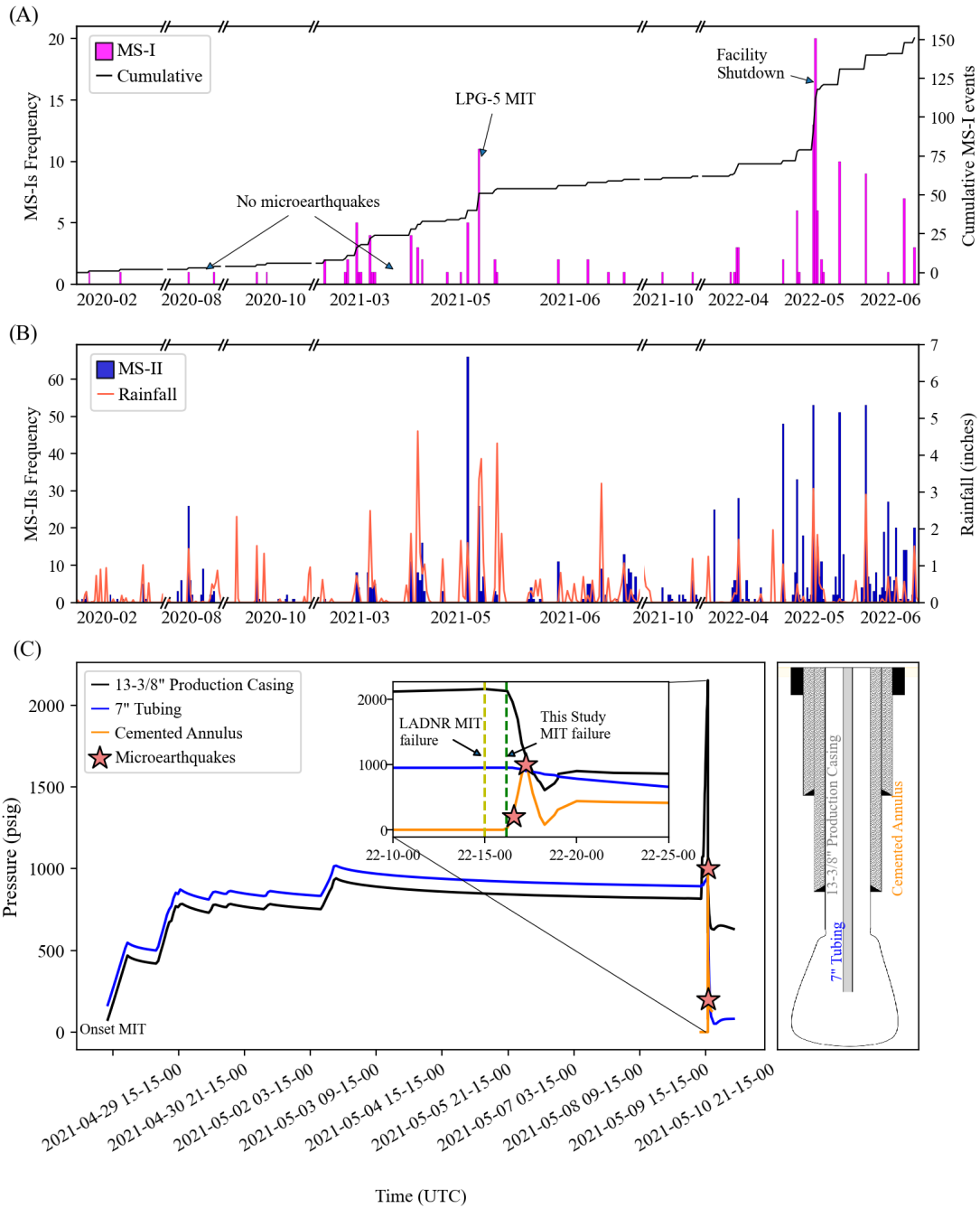
295 Where A_{max} is the maximum displacement in mm, D is the hypocentral distance in km and
 296 $a=0.377$ for events located <40 km from the station (Di Grazia et al., 2001). The local magnitude
 297 for each station was estimated, and the median of all stations was selected as the final magnitude
 298 for each event. Since a magnitude scale has not been developed for the Louisiana Gulf Coast, the
 299 absolute values of the magnitudes may vary, however, they provide a good indication of the
 300 relative size of events.

301 3.4 Focal Mechanisms

302 We computed focal mechanisms for the relocated events by inverting manually picked
 303 first motion P-wave polarity amplitudes. Spectral gates were used to denoise raw waveforms and
 304 improve identification of P-wave polarities ([Figure S6](#)) (Sainburg et al., 2020). A minimum of 8
 305 stations were required for calculating focal mechanisms. We performed a grid search every 5° to
 306 obtain solutions with the HASH program (Hardebeck & Shearer, 2008). Fault plane solution
 307 uncertainties which can be affected by polarity errors, takeoff angles and event location errors,
 308 were calculated by perturbing the input velocity model over multiple iterations.

309 4 Results

310 We use waveform duration, event onset, and apparent velocities to classify the events
 311 detected by our hybrid U-Net model into two main types of microseismic (MS) events and
 312 designated them MS-I and MS-II. The MS-I events have high-frequencies (5 - 40 Hz), and fast
 313 P-wave travel-times of <1 second across the array ([Figure 2 e-f](#)) and their temporal distribution is
 314 shown in [Figure 3a](#). The 152 MS-I events exhibit a combination of emergent and impulsive
 315 waveform onsets with attenuated amplitudes over short distances suggestive of local scattering
 316 and potential absorption from gas-filled caverns. Local magnitudes for these events range
 317 between M_L -3 to 2, with an average magnitude of -1.54, and a median of -1.68. The MS-I events
 318 were relocated using the HYPODD program (Waldhauser, 2001). In contrast, the 1019 MS-II
 319 events ([Figure 3b](#)) have impulsive waveforms ([Figure S7](#)) with slower seismic wave travel-times
 320 of <500 m/s. These events have higher frequencies (70 - 100 Hz) compared to MS-I events and
 321 were not located. The event amplitudes were large enough to be recorded across the dome which
 322 is indicative of a significant energy source.



323

324 **Figure 3.** Temporal distribution of microearthquakes and cavern pressure. (a) Histogram of daily
 325 number of MS-I (microearthquakes) recorded at Sorrento (magenta) showing the mechanical
 326 integrity test (MIT) failure and facility shutdown. (b) Histogram of daily number of MS-II events
 327 (blue) with rainfall overlay (red lines). (c) Pressure profile of the LPG-5 cavern during the MIT
 328 showing coincidence between the microearthquake timing and annulus pressure spike.

329 4.1 Temporal Seismicity Trend

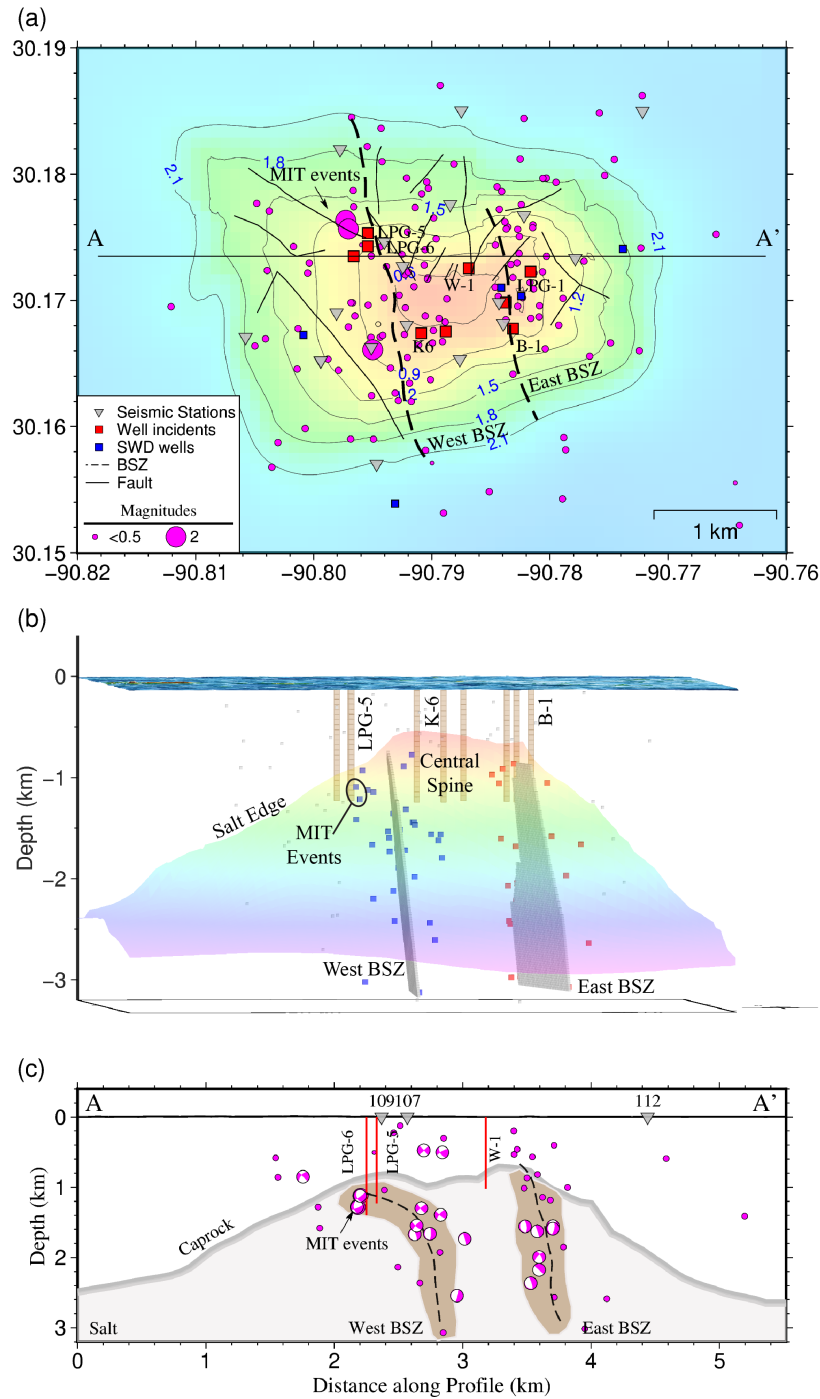
330 The MS-I events exhibit random cascade-like peaks followed by periods of quiescence
331 (Figure 3a). The rate of activity for MS-I was less than 5 events per day for most of the study
332 period, however the seismicity rate doubled on May 10, 2021, when the LPG-5 well failed a
333 mechanical integrity test. We also observed a second spike in the number of microearthquakes
334 when background noise levels decreased due to a facility shutdown and workover activity at the
335 W-5 well (LADNR, 2022b). No aftershock sequences were observed in the catalog which is
336 suggestive of intermittent deformation pulses that weaken over time (Nayak & Dreger, 2018).
337 Swarms of MS-II events were observed to coincide with heavy rainfall periods (Figure 3b), and
338 further investigation into potential sources is planned for a subsequent study.

339 4.2 Local Seismicity along Shear Zones

340 Prior to making any geological interpretations, we evaluated the reliability of the event
341 locations. An event location is considered reliable if it was recorded by a minimum of four
342 stations with computed location errors <50 m and travel time residuals <30 ms. We obtained
343 high-quality hypocenter locations for 129 of the 152 detected MS-I microearthquakes. A large
344 number of events originate within the dome at depths between 0.2 – 4 km, spread out along two
345 zones in a N-S direction, and are separated by a noticeable gap in seismicity around the W-1
346 cavern (Figure 4a). Normal faults above the salt also strike N-S but the clustered events are not
347 aligned along any of these faults. Large magnitude events were detected close to caverns with
348 well incidents (Figure 4a) and few events are observed outside the salt boundaries.

349 The two zones of clustered seismicity (dashed lines in Figure 4a and 4c) have
350 dimensions of ~2 km along strike, that extend to ~1-3 km depth with varying widths. Reports
351 from the LPG-2 well (Looff, 2017), that was drilled between two salt spines and intersects the
352 western cluster of seismicity, confirm the presence of two salt walls that are indicative of
353 boundary shear zones (BSZ) (Figure 5b). We therefore interpret that the two clusters of
354 seismicity are associated with salt movement along boundary shear zones that we abbreviate as
355 the west and east BSZs. Both shear zones have near-vertical dips that are confirmed by the focal
356 mechanism solutions (>80°E).

357 Seismicity along the west BSZ is diffuse and twice as dense as seismicity in the east
358 BSZ. In the east BSZ, the microearthquakes are clustered within a 200 m wide zone (Figure 4c),
359 that is significantly wider than the spatial location uncertainty of ± 50 m and is thus indicative of
360 real features and not location artifacts. The seismicity cluster clearly outlines an almost planar
361 feature that dips to the east (Figures 4c and S2b).

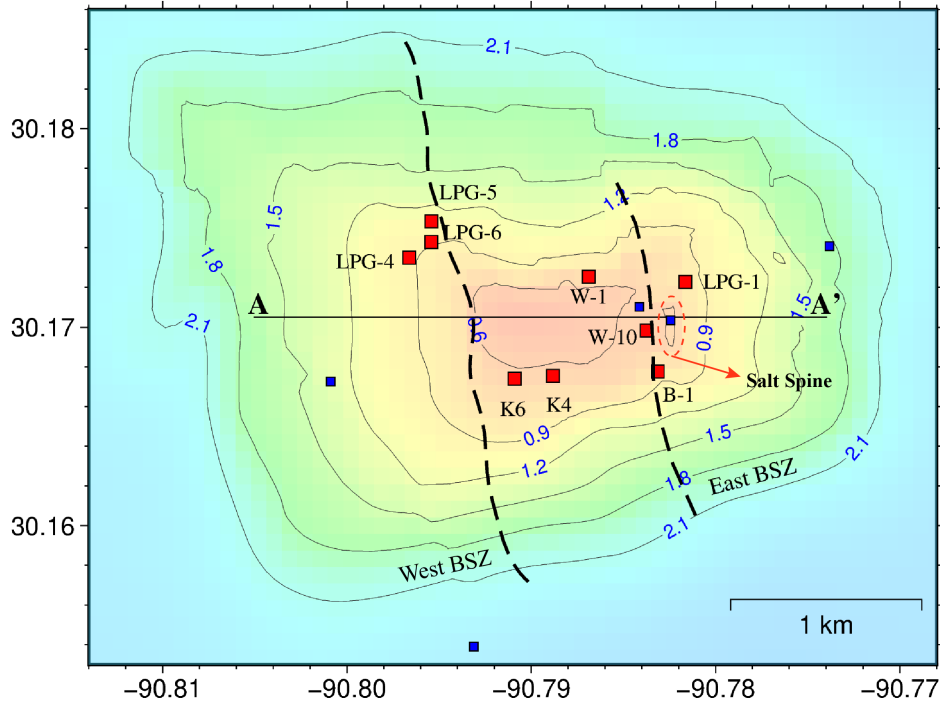


362

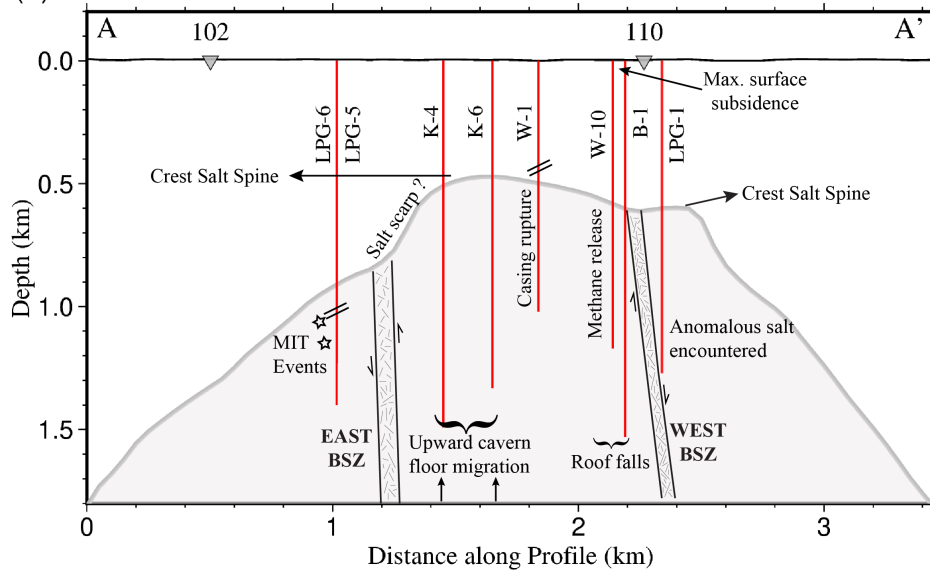
363 **Figure 4.** Microearthquake distribution across the dome. (a) Spatial distribution of
 364 microearthquakes (magenta circles) scaled by their local magnitudes. The east (Looft, 2017) and
 365 west BSZ are shown with black dashed lines. Caprock faults are shown as solid gray lines, and
 366 background shaded contours of the top of salt are modified after Looft (2017). (b) View from the
 367 south showing the three-dimensional salt structure, cavern outlines (yellow), microearthquakes,
 368 and the extent of the two boundary shear zones. Planes of best fit through the clustered
 369 seismicity help to differentiate the boundaries between salt spines. (c) Cross-section A-A'
 370 showing estimated widths of the shear zones based on clustered seismicity. The

371 microearthquakes within 300 m of the profile are shown and the focal mechanisms are viewed
 372 from the south.

(a)



(b)



373

374 **Figure 5.** Independent shear zone identification with well and cavern data. (a) Map view of
 375 caverns with prior incidents relative to shear zone traces. (b) Representative planar features of
 376 shear zones with labeled cavern incidents. Caverns are project onto the cross-section.

377

378 4.3 Focal Mechanisms and Hypocenter Imaging

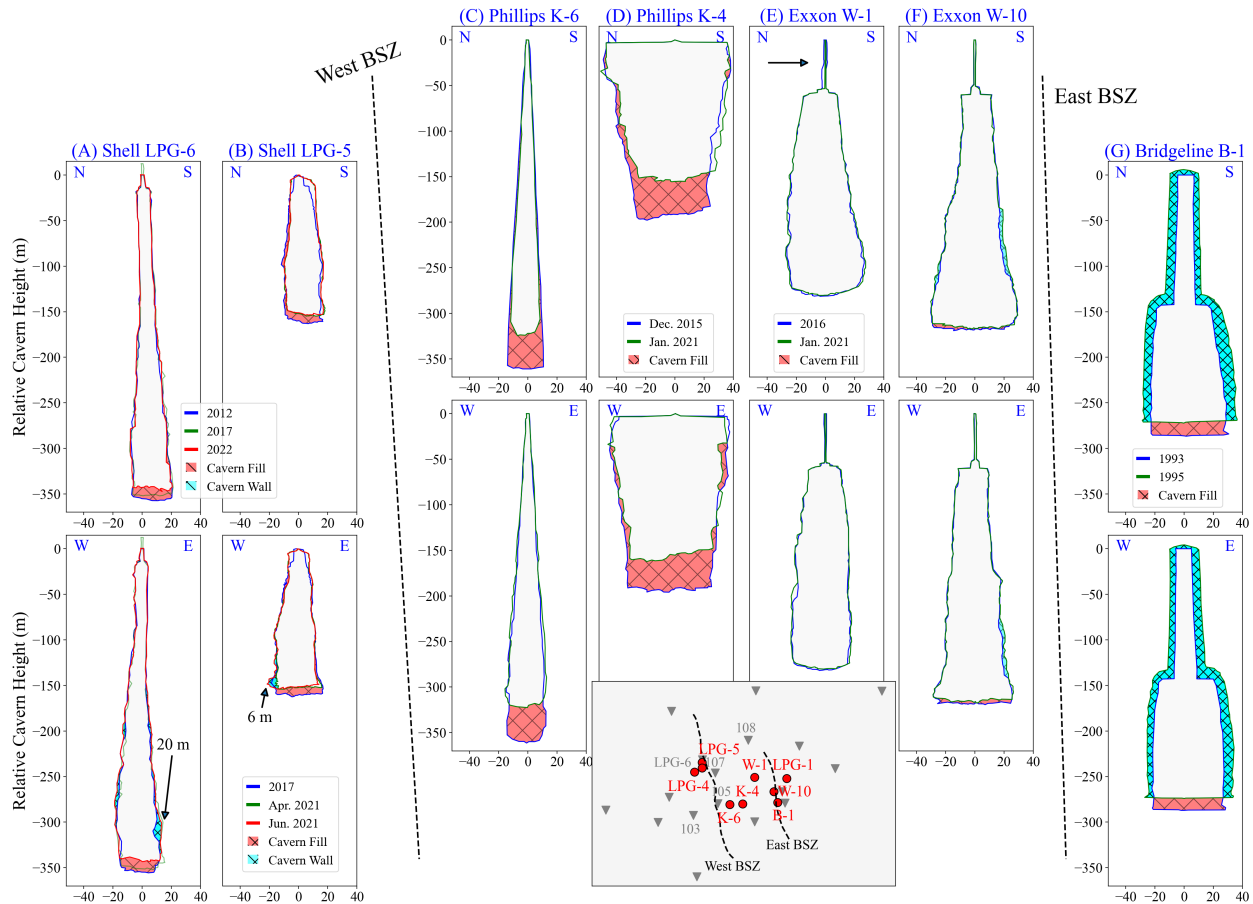
379 Microearthquake focal mechanisms are useful for understanding relative shearing
380 motions. Reliable focal mechanism solutions with maximum azimuthal gaps $\leq 90^\circ$ and
381 maximum takeoff angles $\leq 60^\circ$, were obtained for thirty events. Fourteen events with weighted
382 polarity errors $\leq 15\%$ and station distribution ratios $\geq 50\%$ were classified as improved quality
383 solutions. **Figure S3** shows the uncertainty estimates for the obtained solutions.

384 The microearthquakes were distributed across both boundary shear zones and their focal
385 mechanisms exhibit north-northwest to south-southeast strikes, oblique left-lateral and normal
386 shearing with dominant dips between $50 - 85^\circ$ (Figure 4c). Estimated fault planes from the
387 hypocenter imaging (details in **Text S3**) are aligned parallel to local normal faults that intersect
388 the top of the salt structural model of Looft (2017) (**Figure 4a**), and perpendicular to the regional
389 east-west striking normal faults. The dip angles of $83-86^\circ$ obtained from best fit rupture planes
390 were validated using focal mechanism solutions.

391 4.4 Changes in Cavern Shapes from Sonar Measurements

392 We further investigate intra-salt deformation by comparing time-lapse sonar
393 measurements to estimate the change in cavern volumes through time. Sonar surveys are an
394 expensive way to estimate cavern volumes and cavern operators are required to acquire them
395 every 5 years for routine monitoring or before and after workover activity (SONRIS, 2022). On
396 the western edge of the dome, sonar measurements acquired within the LPG-5 and LPG-6
397 caverns from 2017 to 2021 or 2022 show small floor changes of 6 and 9 m, respectively that
398 translates to an average salt closure rate 1-2 m/year (**Figure 6a-b**). Within the central spine sonar
399 measurements of the K-4 and K-6 caverns acquired in 2015 and 2021 show major changes in
400 cavern floor height of 43 and 40 m, respectively with minimal roof migration (**Figure 5b**; **Figure**
401 **6c-d**). This translates to an average salt closure rate of nearly 8 m/year. The magnitude of salt
402 creep in different spines can influence variations in cavern closure rates, causing some caverns to
403 close faster than others (Bettin et al., 2017; Cyran, 2021), which is evident in the different
404 closure rates observed at these four caverns located less than a kilometer from each other.

405 In the eastern part of the dome, salt creep is not as pronounced, and time-lapse sonar
406 measurements from the B-1 cavern (**Figure 6g**) show evidence of roof falls instead. The cavern
407 roof and sides expand which consequently fills up the cavern floor and is indicative of brittle salt
408 behavior associated with roof falls around the east BSZ. Roof falls have also been reported
409 within the W-10 cavern by operators (**Figure 6f**) (LADNR, 2022a). To the NE, the impact of
410 lateral salt movement can also be observed in sonar measurements of the W-1 cavern (**Figure 6e**)
411 which can cause casing and liner ruptures. These variations in the cavern deformation
412 determined from sonar measurement from west to east across the dome is indicative of
413 differential salt movement across different spines that are separated by shear zones (**Figure 5b**).
414 Transient creep along salt shear zones can lead to large deformations over short periods of time,
415 generating the detected microearthquakes (**Figure 1c-d**; **4b-c**; **5b**) (Cyran, 2021).



416

417 **Figure 6.** Timelapse cross-sections of cavern geometry obtained from sonar measurements
 418 (SONRIS, 2022). All caverns are plotted at the same scale, names are indicated above each
 419 panel, and cavern locations are shown in the inset map. Top panels show N-S cross-sections and
 420 bottom panels show W-E sections, with the legends indicating the year of the sonar surveys.
 421 Changes in the cavern shape through time are indicated with cyan and red patterns

422 4.5 Well Incidents

423 Cavern wells drilled near boundary shear zones (BSZ) and the salt edge are at risk of
 424 developing complications (Bérest et al., 2013; Ford & Dreger, 2020). One such incident along
 425 the west BSZ occurred in the LPG-5 cavern well. The LPG-5 well was drilled between the west
 426 BSZ and salt edge in 1973 and shut-in for several years (Figure 4c and 5b). A mechanical
 427 integrity test (MIT) was performed in 2021 to assess its stability for renewed cavern operations,
 428 and on May 3, 2021, brine was injected to raise the cavern pressure to 6.48 MPa (941.09 psi) in
 429 the production annulus followed by a 7-day stabilization period until the pressure decline
 430 reached 0.03 MPa (5.1 psi) per day (Figure 3c). The cavern lost integrity during the nitrogen
 431 injection phase of the MIT on May 10, 2021, and the casing pressure changed by more than 5%,
 432 which constitutes a well failure incident. Casing pressures dropped from 14.86 MPa (2156 psi) to
 433 4.62 MPa (670 psi) in less than two minutes and site workers recall feeling ground movement,
 434 hearing an audible pop, and observing the release of 220,000 scf of nitrogen at the surface
 435 (LADNR, 2021a). Following the drop in cavern pressures, two MS-I type events occurred at

436 22:16:34.72 UTC and 22:17:11.96 UTC respectively, within proximity of the LPG-5 cavern
437 (MIT events 18 and 19 in A-A' in [Figure 2e; 3c; 4c; 6b](#)), and post-incident reports indicate
438 casing cracks at 1131-1136 m depth around the microearthquake hypocentral depths of 1259 and
439 1149 m respectively (Solutions, 2021). The microearthquakes were located west of the inferred
440 west BSZ core ([Figure 5b](#)), within a potential damage zone where salt shearing can trigger
441 seismicity. Additional damage was identified at the base of the cavern with sonar surveys ([Figure](#)
442 [6b](#)), and a 6-9 m wide by 1.5 m deep crater was observed around the well head (LADNR,
443 2021b).

444 Other incidents near the west BSZ include an emergency workover to replace the brine
445 string in LPG-4 following its failure in Q2 2020 (LADNR, 2020b). Near the east BSZ, our
446 review of historical well reports indicate that liner ruptures were documented three times
447 between 1960-1966 in the W-5 saltwater disposal well (Consultants, 1990). Methane blowouts
448 have also been recorded at the W-9 cavern and anomalous salt deposits were encountered within
449 the LPG-1 and LPG-2 caverns ([Figure 5b](#))(Looff, 2017).

450 4.6 Subsidence Surveys

451 To investigate the effect of salt migration on surface infrastructure, we reviewed
452 subsidence measurements acquired by the salt dome operators between 2015 to 2019. Five
453 precision level surveys were conducted using a combination of 57 monuments and wellheads
454 (USA, 2019). We estimated relative subsidence by measuring the elevation differences between
455 a reference benchmark (SD-01 monument) and the level-survey monuments. Changes in annual
456 elevation were derived from elevation differences and a subsidence map was generated by
457 linearly interpolating points between monuments ([Figure S5](#)). A maximum subsidence of ~0.81
458 inches/year was observed west of the eastern BSZ around the Kaiser 1 well which is plugged and
459 abandoned (LADNR, 1986), and 320 m southwest of the Bridgeline B-1 cavern. Other notable
460 caverns with high rates of elevation change include LPG-5, W-4, W-6, and W-7 ([Figure S1](#)). All
461 these caverns occur within proximity of the shear zones, and the brittle behaviour of anomalous
462 salt can accelerate roof falls, which influences surface subsidence if cavern pressures are not
463 properly managed. At the time of writing, no surface facilities face critical endangerment but
464 periodic monitoring of these caverns are recommended even after they have been plugged and
465 abandoned.

466 5 Discussion

467 In this section, we combine observations from our microearthquake catalog with
468 associated well data. We analyze the variations in seismicity across the salt dome and evaluate
469 potential source mechanisms. We proceed to integrate the spatial and temporal seismicity
470 patterns with the geological context around the salt dome which helps us unlock new insights
471 and evaluate the contributions of our dataset and methods.

472 5.1 Microearthquake Source Mechanisms in Salt domes

473 Previous studies have investigated the factors that can trigger microearthquakes in salt-
474 domes. E.g., at the Cerville-Buissoncourt salt mine in France, more than 200 events per hour
475 were reported following the M_w 7.2 Kepulauan Talaud earthquake in Indonesia, and it was
476 concluded that the events were triggered by passing surface waves (Jousset & Rohmer, 2012).

477 We investigate the possibility of triggering from passing surface waves from remote-large
478 earthquakes by analyzing 1820 teleseismic earthquakes with magnitudes $M_w > 5$ that occurred
479 during the monitoring period. On the day of the well failure (May 10, 2021), three teleseismic
480 events (M_w 5-5.4, located $82 - 115^\circ$ away) occurred within 5 minutes of the well failure,
481 however our seismic array did not detect the ground motion. Analysis of regional earthquake
482 catalogs show that large events occur almost daily, in contrast to our local catalog of
483 microearthquakes that exhibit cascade-like peaks in seismicity separated by several days of no
484 activity (Figures 3a-b). Subsequently, we did not find evidence of our observed
485 microearthquakes being triggered by passing surface waves from of remote large earthquakes.

486 For caverns located close to the edge of the salt-sediment boundary, caprock movement
487 from salt creep near the boundary can trigger microearthquakes (Fortier et al., 2006) and in
488 extreme cases, sidewall cavern collapse can trigger microearthquakes as sediments flow along
489 the disturbed rock zone into breached caverns (Chicago Bridge, 2013; Ford & Dreger, 2020).
490 However, our cross-section of the salt structural map with projected microearthquakes located
491 within 300 m (Figure 4c) shows that few events occur near the salt-sediment boundary. But the
492 majority of the microearthquakes occur deeper within the dome. The sonar surveys of caverns
493 close to the salt edge (< 125 m, LPG-5 and 6) show no indications of major sidewall damage
494 (Figure 6a-b) and the subsidence values above those caverns (Figure S5) are within relatively
495 safe thresholds (USA, 2019). While the predominant source mechanism for the identified events
496 does not appear to be caprock movement or sidewall collapse, we advocate for the continuous
497 seismic and sonar monitoring of the LPG-5 cavern considering that it sustained sidewall damage
498 during the well failure event (Figure 6b), and its proximity to the salt-sediment boundary (Figure
499 5b).

500 We investigated the plausibility of the microearthquakes being generated by roof falls
501 within the caverns. Roof falls modify the geometry of caverns and can be monitored using sonar
502 surveys. Falling blocks of salt or overlying sediment in caverns generate high frequency
503 microearthquakes upon impact with the bottom of the cavern that can be recorded by nearby
504 seismometers. The soluble portions of the blocks are dissolved in cavern brines while the
505 insoluble blocks fill the base of the cavern. This effect has been observed at the Geosel-
506 Manosque, Cerville-Buissoncourt, Verkhnekamskoye salt deposits in Europe, and sinkholes
507 around the Dead Sea region (Fortier et al., 2006; Malovichko, 2009; Mercerat et al., 2009; Wust-
508 Bloch & Joswig, 2006). For example, well logs at the Cerville-Buissoncourt dome recorded a
509 roof migration of 6 m in one year, and a final roof height difference of 25 m over the operating
510 period of the cavern. At Sorrento, timelapse sonar surveys of the B-1 cavern revealed a 4 m roof
511 migration and 6 m wall widening before its abandonment, and roof falls were reported in the W-
512 10 cavern (Figure 5b and 6f-g) (LADNR, 2022a). These observations suggest possible block
513 drop seismicity. However, the location of our microearthquakes at depths below and outside the
514 caverns (Figure 4b), along with sonar surveys in other caverns displaying relative roof stability
515 while exhibiting cavern floor migration (Figure 6a-d) implies the existence of other source
516 mechanisms within the Sorrento dome.

517 Although rocks falling from the roof cannot explain upward cavern floor migration with a
518 stable roof, upward salt migration, which contributes to increased cavern closure rates can
519 explain these observations (Bérest et al., 2013). The clustered microearthquakes align with
520 mapped shear zones from drilled wells (Figure 4c; 5b), where salt creep reactivates preexisting

521 fractures in anomalous salt bodies (Davison, 2009) (Figure 1d). Salt creep along a shear zone is
522 capable of overstretching well casing, causing the casing and liner ruptures observed in the LPG-
523 4, LPG-5, W-1 and W-5 wells (Figure 5 and 6). Salt creep and shear zone deformation within
524 salt domes have been linked to gas outbursts, increased shearing, slickensides occurrence, and
525 halite recrystallization at other Gulf Coast domes (Bérest et al., 2019; Davison, 2009; Neal et al.,
526 1993). At Sorrento, drilled wells within the vicinity of the shear zones were reported to have
527 methane outbursts, anomalous salt properties, and ruptured well casings (Looff, 2017). This
528 suggests that internal shearing of salt is the dominant source of microearthquake activity at the
529 Sorrento dome.

530 5.2 Effect of Salt Creep on Shear Zones

531 While the concept of salt creep is well understood and even accounted for in
532 geomechanical models (Sandia, 2017), shear zone identification and its potential hazards are
533 poorly understood and often overlooked. During normal storage operations, wellhead pressure
534 steadily increases in caverns due to salt creep, and this pressure is usually bled off when it
535 exceeds the operating pressure range as part of a pressure cycle (Bettin et al., 2017). During
536 workovers, the caverns are completely depressurized, which can result in accelerated salt creep
537 along the shear zones (Bérest et al., 2013). Salt creep along the shear zones can trigger
538 microearthquakes, increasing the risk of casing breach and gas release during well workovers
539 like a mechanical integrity test. Based on the proximity of the LPG-5 cavern to the west BSZ
540 (Figure 4c and 5b) and the low cavern pressures during the workover process, we conclude that
541 accelerated shear movement weakened the well casing to the point of failure following which
542 impulsive energy from the MIT events exacerbated the damage (Figure 3c), resulting in the gas
543 release observed at the surface, and associated wellhead damage.

544 5.3 Geological Context of Salt Dome Seismic Hazards

545 When assessing seismic hazard, we need to evaluate all the available subsurface data.
546 Well logs, sonar measurements and hanging string failure events are useful for monitoring
547 cavern integrity at specific points in time. However, due to data sparsity (acquisition timeframe
548 and limited sample points), it is difficult to use them to independently assess unstable regions
549 within the salt dome unless an obvious failure occurs (Ehgartner & Sobolik, 2009). In contrast
550 seismicity is useful for mapping the 3D extent of shear zones, identifying weak zones that are
551 actively undergoing seismic deformation (seismogenic regions), and improving near real-time
552 hazard mapping in salt dome cavern facilities (Mercerat et al., 2009). Independently both data
553 types provide distinct advantages. However, together they can be integrated to robustly assess
554 seismic hazards. For instance, when the microearthquakes are integrated with well data, the dip
555 of the east BSZ microearthquakes explains how the LPG-1 and LPG-2 wells encountered
556 anomalous salt deposits considering they were drilled east of the shear zone (Figure 5b). The
557 gaps in seismicity between the two BSZs suggest 3 potential spines migrating upwards at
558 different rates. The central salt spine is migrating the fastest, as evidenced by the high cavern
559 closure rates within the K-4 and K-6 caverns (Figure 6c-d), and the relatively thinner overburden
560 thickness above the spine. To the east and west, the other salt spines are much smaller and
561 relegated to the flanks of the central spine. Considering salt spines discussed in literature are
562 circular in shape (Warren, 2016), we could have E-W trending shear zones that were not imaged
563 in our current catalog. Additional months of seismic monitoring can be combined with downhole

564 sensors to improve the number of intra-salt event detections, and accuracy of events locations for
565 further shear zone imaging.

566 For operators, temporal seismicity trends can provide insights into salt instability during
567 workover or drilling operations. However, interpreters have to be careful when analyzing such
568 trends. While a departure from background seismicity trends can be indicative of impending
569 damage, time to failure models cannot be derived from seismicity alone (Ford & Dreger, 2020;
570 Petersen et al., 2006). The number of recorded events depends on noise levels, salt creep, and
571 station distribution as evidenced by the higher number of daily recorded microearthquakes
572 during the facility shut-down in comparison to the LPG-5 well failure event (Figure 3a). In this
573 study, our integration of seismic and well data allows us to associate event spikes with well
574 incidents and improve our understanding of hazard at the Sorrento salt dome.

575 Considering the distance to the salt edge and microseismicity distribution, we propose
576 that the safest region for cavern operations is above the central spine, between the two identified
577 BSZs at depths <1.3 km (Figure 4b). Caverns located on the flanks away from the central spine
578 are closer to the salt edge which increases the risk of additional complications during operations.
579 One draw-back for leaching the central spine is the high surface subsidence near the shear zones,
580 and fast closure rate observed in the K-4 and K-6 caverns (Figure 5b; 6c-d). Additional cavern
581 wells will need to avoid those regions to minimize associated subsurface hazards. By avoiding
582 the salt around the shear zones, the risk of casing breach due to seismicity is relatively lower.

583 As more salt domes are enlisted for energy storage as part of the energy transition, the
584 environmental safety of cavern operations becomes increasingly crucial. Integrating
585 microseismic monitoring into site evaluation criteria for new sites and deploying a combination
586 of borehole and surface nodal arrays for passive monitoring of existing underground storage
587 facilities are key strategies. These approaches enable operators to proactively identify ground
588 movement on seismic instruments and take steps to minimize the risk of blowouts or sinkhole
589 formation.

590 **6 Conclusion**

591 Similar to other machine learning earthquake detection models (Mousavi et al., 2020;
592 Ross et al., 2018; Zhu & Beroza, 2019), we detect microearthquakes using 3-component
593 waveforms however, our model is more efficient at detecting salt dome microearthquakes
594 because it was trained and finetuned with small microearthquakes ($M_w < 3$) from both tectonic
595 and salt dome environments. We successfully apply our Hybrid U-Net machine learning model
596 for microearthquake detection at the Sorrento salt dome, and combined our event catalog with
597 existing well data and published literature to generate a holistic assessment of seismic hazard.
598 The detected events with magnitudes ranging between $M_L -3$ to 2 were correlated with salt creep
599 and fracture reactivation along two internal boundary shear zones where seismicity triggers
600 cavern deformation. Our geological interpretation accurately explains past and recent incidents,
601 and we propose recommendations to improve the safety of cavern operations.

602 Our pre-trained machine learning model is easy to use and can be finetuned to monitor
603 other sites with limited seismicity catalogs such as nuclear plants, dams, bridges. It is also useful
604 for detecting seismicity from other hazards such as landslides and mine collapses, and
605 identifying BSZs at other sites used for underground storage. BSZ identification is of central
606 importance if salt domes are to be utilized for hydrogen storage during the energy transition

607 because hydrogen has lower molecular weight than natural gas and can escape into even smaller
608 cracks. In this study, we have demonstrated that salt dome characterization can be optimized
609 with microearthquake monitoring to identify seismogenic BSZs prior to leaching salt caverns,
610 allowing preferential location of caverns within stable salt which extends their lifecycles when
611 used for natural gas and hydrogen storage.

612 **Acknowledgments**

613 We thank the operators at the Sorrento salt dome in Ascension Parish, Louisiana for providing
614 access to the sites occupied by our seismic array. We are grateful to Justin Kain and Jeff Nunn
615 for their help installing instruments, and Jeff Hanor for discussions on the salt domes. We thank
616 the USGS Lower Mississippi-Gulf Water Science Center for releasing the preliminary data from
617 the Bayou Conway station. Most computations were carried out on the LSU HPC SuperMike II
618 cluster. Some of the seismic instruments were provided by the United States Geological Survey
619 and Earthscope through the Earthscope Primary Instrument Center (EPIC, formerly the
620 PASSCAL Instrument Center) at New Mexico Tech. This material is based upon work supported
621 by the National Science Foundation under Grant No. (2045983). The facilities of the Earthscope
622 Consortium are supported by the National Science Foundation's Seismological Facilities for the
623 Advancement of Geoscience (SAGE) Award under Cooperative Support Agreement EAR-
624 1851048.

625 **Open Research**

626 All data needed to evaluate the conclusions in the paper are present in the paper and/or
627 Supporting Information. The waveform data from the Sorrento array are publicly available at the
628 SAGE Facility Web Services (<https://service.iris.edu/irisws/>) under the ZE network (Persaud,
629 2020). The trained model used for event detection, catalogs of the detected events, and scripts to
630 reproduce the images are available at the Zenodo repository
631 <https://doi.org/10.5281/zenodo.10799264>. For review purposes, the repository can be accessed
632 with a unique token link.
633 Data analysis was carried out using different python packages. ObsPy was used for processing
634 the seismic data (Krischer et al., 2017). All plots were created with Matplotlib and PyGMT 6.0.0
635 (Hunter & Dale, 2007; Uieda et al., 2021). The hybrid autoencoder model was built with
636 TensorFlow 2.5, and shapefiles were processed using Geopandas (Abadi et al., 2015; Jordahl et
637 al., 2020).

638 **References**

- 639 Abadi, M., Agarwal, A., Barham, P., Brevdo, E., Chen, Z., Citro, C., Corrado, G. S., Davis, A., Dean, J., & Devin,
640 M. (2015). TensorFlow: Large-scale machine learning on heterogeneous systems.
- 641 Bauer, S. J., Ehgartner, B. L., & Neal, J. T. (1997). *Geotechnical studies associated with decommissioning the*
642 *strategic petroleum reserve facility at Weeks Island, Louisiana: a case history* (by Sandia National
643 Lab.(SNL-NM), Albuquerque, NM (United States)).
644 <https://digital.library.unt.edu/ark:/67531/metadc677438/>.
- 645 Beckman, K., Determeyer, P., & Mowrey, E. (1995). *Natural gas storage: Historical development and expected*
646 *evolution. Final report, December 1994-February 1995*.
647 <https://ntrl.ntis.gov/NTRL/dashboard/searchResults/titleDetail/PB95249900.xhtml#>.
- 648 Bérest, P., Djakeun-Djizanne, H., Brouard, B., & Hévin, G. (2013). *Rapid Depressurizations: Can they lead to*
649 *irreversible damage?* Solution Mining Research Institute Spring 2012 Technical Conference,
650 <https://doi.org/10.48550/arXiv.1302.2582>
- 651 Bérest, P., Réveillère, A., Evans, D., & Stöwer, M. (2019). Review and analysis of historical leakages from storage
652 salt caverns wells. *Oil & Gas Science and Technology–Revue d'IFP Energies nouvelles*, 74, 27.
653 <https://doi.org/10.2516/ogst/2018093>
- 654 Bettin, G., Hart, D., Sobolik, S. R., Park, B., & Lord, A. C. S. (2017). *Depressurization Effects in Salt Dome*
655 *Caverns*.
- 656 Caglayan, D. G., Weber, N., Heinrichs, H. U., Linßen, J., Robinius, M., Kukla, P. A., & Stolten, D. (2020).
657 Technical potential of salt caverns for hydrogen storage in Europe. *International Journal of Hydrogen*
658 *Energy*, 45(11), 6793-6805.
- 659 Chicago Bridge, I. C. C. I. (2013). *Blue Ribbon Commission Initial Technical Briefing, Louisiana State University, 5*
660 *April 2013*.
661 http://www.dnr.louisiana.gov/assets/OC/BC_All_Updates/Plans_Reports/BlueRibb.04.05.13.pdf.
- 662 Consultants, W.-C. (1990). *Injection Well Investigation Workplan* [Report](970152). (submitted to Exxon Pipeline
663 Company Sorrento Facility, Louisiana).
664 https://ucmwww.dnr.state.la.us/ucmsearch/UCMRedir.aspx?url=http%3a%2f%2fucmprod%3a16200%2fcs%2fidcplg%3fdService%3dGET_FILE%26dDocName%3d14268206%26Rendition%3dWeb%26RevisionSelectionMethod%3dLatest. (last accessed January, 2023)
- 666 Cyran, K. (2021). The influence of impurities and fabrics on mechanical properties of rock salt for underground
667 storage in salt caverns—a review. *Archives of Mining Sciences*, 66(2), 155-179.
- 668 Davison, I. (2009). Faulting and fluid flow through salt. *Journal of the Geological Society*, 166(2), 205-216.
669 <https://doi.org/10.1144/0016-76492008-064>
- 670 Di Grazia, G., Langer, H., Ursino, A., Scarfi, L., & Gresta, S. (2001). On the estimate of earthquake magnitude at a
671 local seismic network. *Annals of Geophysics*, 44(3). <https://doi.org/10.4401/ag-3577>.
- 672 Dreger, D. S., & Ford, S. R. (2020). Pre-Sinkhole Seismicity at the Napoleonville Salt Dome: Implications for Local
673 Seismic Monitoring of Underground Caverns. *Seismological Research Letters*, 91(3), 1672-1678.
674 <https://doi.org/10.1785/0220190224>
- 675 Ehgartner, B., Neal, J., & Hinkebein, T. (1998). *Gas releases from salt*. A. Sandia National Lab.(SNL-NM), NM
676 (United States). doi.org/10.2172/656531.
- 677 Ehgartner, B. L., & Sobolik, S. R. (2009). *Analysis of cavern stability at the West Hackberry SPR site*.
678 <https://www.osti.gov/servlets/purl/959096>.
- 679 EIA. (2012). *Natural Gas Interstate and Intrastate Pipelines* EIA from FERC and other external sources.
680 eia.gov/maps/map_data/NaturalGas_InterIntrastate_Pipelines_US_EIA.zip
- 681 Evans, D. (2007). An appraisal of Underground Gas Storage technologies and incidents, for the development of risk
682 assessment methodology. Volume 1, Text. Volume 2, Figures and Tables.
- 683 Evans, D. J., & Schultz, R. A. (2017). Analysis of occurrences at underground fuel storage facilities and assessment
684 of the main mechanisms leading to loss of storage integrity. ARMA US Rock Mechanics/Geomechanics
685 Symposium,
686
- 687 Ford, S. R., & Dreger, D. S. (2020). Pre-Sinkhole Seismicity at the Napoleonville Salt Dome: Implications for Local
688 Seismic Monitoring of Underground Caverns. *Seismological Research Letters*, 91(3), 1672-1678.
689 <https://doi.org/10.1785/0220190224>

- 745 [%2fidcplg%3fldcService%3dGET_FILE%26dDocName%3d13729513%26Rendition%3dWeb%26RevisionSelectionMethod%3dLatest](#). (last accessed June, 2022)
- 746
- 747 LADNR. (2021b). *Class II Well Test / Inspection Report at LPG-05 on 19 May 2021* [FORM UIC-7](971518).
748 (submitted to the Louisiana Department of Natural Resources, Office of Conservation, Injection and
749 Mining Division).
750 https://ucmwww.dnr.state.la.us/ucmsearch/UCMRedir.aspx?url=http%3a%2f%2fucmprod%3a16200%2fcs%2fidcplg%3fldcService%3dGET_FILE%26dDocName%3d13729514%26Rendition%3dWeb%26RevisionSelectionMethod%3dLatest. (last accessed June, 2022)
- 751
- 752
- 753 LADNR. (2022a). *LPG W-10 Log Interpretation Summary and Certification Report* [Report](971569). (submitted to
754 the Louisiana Department of Natural Resources, Office of Conservation, Injection and Mining Division).
755 https://ucmwww.dnr.state.la.us/ucmsearch/UCMRedir.aspx?url=http%3a%2f%2fucmprod%3a16200%2fcs%2fidcplg%3fldcService%3dGET_FILE%26dDocName%3d14475696%26Rendition%3dWeb%26RevisionSelectionMethod%3dLatest. (last accessed August, 2022)
- 756
- 757
- 758 LADNR. (2022b). *LPG W-10 Salt Cavern Weekly Monitoring Log and Summary Report for Q2 2022* [FORM UIC-
759 50](971569). (submitted to the Louisiana Department of Natural Resources, Office of Conservation,
760 Injection and Mining Division).
761 https://ucmwww.dnr.state.la.us/ucmsearch/UCMRedir.aspx?url=http%3a%2f%2fucmprod%3a16200%2fcs%2fidcplg%3fldcService%3dGET_FILE%26dDocName%3d14088271%26Rendition%3dWeb%26RevisionSelectionMethod%3dLatest. (last accessed June, 2022)
- 762
- 763
- 764 Loeff, K. (2017). The Impact of Anomalous Salt and Boundary Shear Zones on Salt Cavern Geometry, Cavern
765 Operations, and Cavern Integrity. Proc. SMRI Spring Meeting, Albuquerque, New Mexico,
- 766 Lord, A. S. (2009). *Overview of geologic storage of natural gas with an emphasis on assessing the feasibility of
767 storing hydrogen*. <https://www.osti.gov/biblio/975258>.
- 768 Malovichko, D. (2009). Study of the seismic source mechanisms in mines of the Verkhnekamskoye potash deposit,
769 in Proc. 7th Int. Symp. on Rockbursts and Seismicity in Mines: Controlling Seismic Hazard and
770 Sustainable Development of Deep Mines (ed. Tang, C.).
- 771 Mercerat, E. D., Driad-Lebeau, L., & Bernard, P. (2009). Induced Seismicity Monitoring of an Underground Salt
772 Cavern Prone to Collapse. *Pure and Applied Geophysics*, 167(1-2), 5-25. <https://doi.org/10.1007/s00024-009-0008-1>
- 773
- 774 Mitchell, D. (2018). *Judge: Fault for Bayou Corne sinkhole lies with Texas Brine, OxyChem, Vulcan; companies
775 had decades of warnings*. The Advocate. Retrieved October 2023 from
776 https://www.theadvocate.com/baton_rouge/news/article_7856ff5e-f4ae-11e7-b86c-4f261682612b.html
- 777 Mousavi, S. M., Ellsworth, W. L., Zhu, W., Chuang, L. Y., & Beroza, G. C. (2020). Earthquake transformer—an
778 attentive deep-learning model for simultaneous earthquake detection and phase picking. *Nature
779 communications*, 11(1), 1-12. <https://doi.org/10.1038/s41467-020-17591-w>
- 780 Mousavi, S. M., Sheng, Y., Zhu, W., & Beroza, G. C. (2019). STANford EArthquake Dataset (STEAD): A global
781 data set of seismic signals for AI. *IEEE Access*, 7, 179464-179476.
782 <https://doi.org/10.1109/ACCESS.2019.2947848>
- 783 Nayak, A., & Dreger, D. S. (2018). Source inversion of seismic events associated with the sinkhole at Napoleonville
784 salt dome, Louisiana using a 3-D velocity model. *Geophysical Journal International*, 214(3), 1808-1829.
785 <https://doi.org/https://doi.org/10.1093/gji/ggy202>
- 786 Nayak, A. D., D. S. (2014). Moment Tensor Inversion of Seismic Events Associated with the Sinkhole at
787 Napoleonville Salt Dome, Louisiana. *Bulletin of the Seismological Society of America*, 104(4), 1763-1776.
788 <https://doi.org/10.1785/0120130260>
- 789 Neal, J. T., Magorian, T., Thoms, R., Autin, W., McCulloh, R., Denzler, S., & Byrne, K. (1993). *Anomalous zones
790 in Gulf Coast salt domes with special reference to Big Hill, TX, and Weeks Island, LA*.
- 791 Neal, J. T., & Myers, R. E. (1994). *Salt dissolution sinkhole at the Weeks Island, Louisiana, strategic petroleum
792 reserve storage site by Sandia National Labs., Albuquerque, NM (United States)* (submitted to the
793 Department of Energy, US.). <https://www.osti.gov/servlets/purl/10106436>.
- 794 Oktay, O., Schlemper, J., Folgoc, L. L., Lee, M., Heinrich, M., Misawa, K., Mori, K., McDonagh, S., Hammerla, N.
795 Y., & Kainz, B. (2018). Attention u-net: Learning where to look for the pancreas. *arXiv preprint
796 arXiv:1804.03999*.
- 797 Persaud, P. (2020). *Monitoring Seismicity in Louisiana [Data set]*. *International Federation of Digital Seismograph
798 Networks* (2045983; International Federation of Digital Seismograph Networks.
799 https://doi.org/doi.org/10.7914/SN/ZE_2020

- 800 Petersen, T., Caplan-Auerbach, J., & McNutt, S. R. (2006). Sustained long-period seismicity at Shishaldin Volcano,
801 Alaska. *Journal of Volcanology and Geothermal Research*, 151(4), 365-381.
- 802 Petroleum, L. (2009). *Leed Successfully Flow Tests Sorrento Salt Dome in Louisiana*. Rigzone. Retrieved October
803 2023 from
804 [https://www.rigzone.com/news/oil_gas/a/80374/leed_successfully_flow_tests_sorrento_salt_dome_in_lou
805 siana/](https://www.rigzone.com/news/oil_gas/a/80374/leed_successfully_flow_tests_sorrento_salt_dome_in_louisiana/)
- 806 Plimpton, H., Foster, R., Risbeck, J., Rutherford, R., King, F., Buffington, G., & Traweck, W. (1980). *Final Report
807 of Mine Explosion Disaster, Belle Isle Mine, Cargill, Inc.*
808 https://books.google.com/books/about/Final_report_of_mine_explosion_disaster.html?id=eOJ8_p1eFoC.
- 809 Rautman, C. A., Loeff, K. M., & Loeff, K. M. (2010). *A Three-Dimensional Geometric Model of the Bayou
810 Choctaw Salt Dome Southern Louisiana Using 3-D Seismic Data by Sandia National Lab. (SNL-NM),
811 Albuquerque, NM (United States)* (submitted to the US Department of Energy National Nuclear Security
812 Administration (NNSA)). <https://www.osti.gov/servlets/purl/1124260>.
- 813 Ronneberger, O., Fischer, P., & Brox, T. (2015). U-net: Convolutional networks for biomedical image segmentation.
814 International Conference on Medical image computing and computer-assisted intervention,
815 https://link.springer.com/content/pdf/10.1007/978-3-319-24574-4_28.pdf
- 816 Ross, Z. E., Meier, M. A., Hauksson, E., & Heaton, T. H. (2018). Generalized Seismic Phase Detection with Deep
817 Learning Short Note. *Bulletin of the Seismological Society of America*, 108(5A), 2894-2901.
818 <https://doi.org/doi.org/10.1785/0120180080>
- 819 Sainburg, T., Thielk, M., & Gentner, T. Q. (2020). Finding, visualizing, and quantifying latent structure across
820 diverse animal vocal repertoires. *PLoS computational biology*, 16(10), e1008228.
- 821 Sandia, G. (2017). *Sorrento Dome, Ascension Parish Louisiana - Geomechanical Assessment Of Shell LPG #3, #4,
822 #5 And #6 (SOE160297-RPT-0003)*. (submitted to the Louisiana Department of Natural Resources, Office
823 of Conservation, Injection and Mining Division). (last accessed June, 2022)
- 824 Schlumberger. (2004). *ExxonMobil Sorrento Salt Dome SWD 13 Sonic Well Log [Well Log](971518)*.
825 [https://ucmwww.dnr.state.la.us/ucmsearch/findAllDocuments.aspx?brief=False&query=xwellserialnumber
826 +LIKE+%27973228%27+&format=HTML&sortfield=xdate&startrow=1#](https://ucmwww.dnr.state.la.us/ucmsearch/findAllDocuments.aspx?brief=False&query=xwellserialnumber+LIKE+%27973228%27+&format=HTML&sortfield=xdate&startrow=1#). (last accessed June, 2022)
- 827 Seni, S., Mullican III, W., & Hamlin, H. (1984). *Texas salt domes—Natural resources, storage caverns, and
828 extraction technology: The University of Texas at Austin, Bureau of Economic Geology, report prepared
829 for Texas Department of Water Resources under interagency contract no* (Texas Department of Water
830 Resources). <https://www.beg.utexas.edu/files/publications/contract-reports/CR1985-Seni-1.pdf>.
- 831 Solutions, C. (2021). *Updated Wellbore Schematic Diagram (WSD) – July 2021 LPG STORAGE 005 (SN 971518)*.
832 (submitted to the Louisiana Department of Natural Resources, Office of Conservation, Injection and
833 Mining Division).
834 [https://ucmwww.dnr.state.la.us/ucmsearch/UCMRedir.aspx?url=http%3a%2f%2fucmprod%3a16200%2fcs
835 %2fidcplg%3fidcService%3dGET_FILE%26dDocName%3d13855784%26Rendition%3dWeb%26Revisio
836 nSelectionMethod%3dLatest](https://ucmwww.dnr.state.la.us/ucmsearch/UCMRedir.aspx?url=http%3a%2f%2fucmprod%3a16200%2fcs%2fidcplg%3fidcService%3dGET_FILE%26dDocName%3d13855784%26Rendition%3dWeb%26RevisionSelectionMethod%3dLatest). (last accessed June, 2022)
- 837 SONRIS, L. (2022). *Louisiana Department of Natural Resources - Strategic Online Natural Resources Information
838 system (SONRIS)*. Retrieved October 2023 from <https://www.sonris.com/>
- 839 SPR, U. D. (2022). *United States Department of Energy - Strategic Petroleum Reserves*. Retrieved October 2023
840 from <https://www.energy.gov/fe/services/petroleum-reserves/strategic-petroleum-reserve/spr-storage-sites>
- 841 Truttmann, S., Diehl, T., & Herwegh, M. (2023). Hypocenter-based 3D Imaging of Active Faults: Method and
842 Applications in the Southwestern Swiss Alps. *Journal of Geophysical Research: Solid Earth*,
843 e2023JB026352.
- 844 Uieda, L., Tian, D., Leong, W., Toney, L., Schlitzer, W., Grund, M., Newton, D., Ziebarth, M., Jones, M., &
845 Wessel, P. (2021). PyGMT: A Python interface for the generic mapping tools.
846 <https://doi.org/doi.org/10.5281/zenodo.5607255>
- 847 USA, W. (2019). *Precision Level Surveys and Subsidence Analysis, Sorrento Salt Dome, 2019 Report (WSP-0513)*.
848 (submitted to the Louisiana Department of Natural Resources, Office of Conservation, Injection and
849 Mining Division).
850 [https://ucmwww.dnr.state.la.us/ucmsearch/UCMRedir.aspx?url=http%3a%2f%2fucmprod%3a16200%2fcs
851 %2fidcplg%3fidcService%3dGET_FILE%26dDocName%3d13406559%26Rendition%3dWeb%26Revisio
852 nSelectionMethod%3dLatest](https://ucmwww.dnr.state.la.us/ucmsearch/UCMRedir.aspx?url=http%3a%2f%2fucmprod%3a16200%2fcs%2fidcplg%3fidcService%3dGET_FILE%26dDocName%3d13406559%26Rendition%3dWeb%26RevisionSelectionMethod%3dLatest). (last accessed June, 2022)
- 853 Waldhauser, F. (2001). hypoDD--A program to compute double-difference hypocenter locations.
854 <https://academiccommons.columbia.edu/doi/10.7916/D8P276P1/download>

- 855 Warren, J. K. (2016). *Evaporites: A geological compendium* (2 ed.). Springer. [https://doi.org/10.1007/978-3-319-](https://doi.org/10.1007/978-3-319-13512-0)
856 [13512-0](https://doi.org/10.1007/978-3-319-13512-0)
- 857 Warren, J. K. (2017). Salt usually seals, but sometimes leaks: Implications for mine and cavern stabilities in the
858 short and long term. *Earth-science reviews*, 165, 302-341. <https://doi.org/10.1016/j.earscirev.2016.11.008>
- 859 Wust-Bloch, G. H., & Joswig, M. (2006). Pre-collapse identification of sinkholes in unconsolidated media at Dead
860 Sea area by 'nanoseismic monitoring' (graphical jackknife location of weak sources by few, low-SNR
861 records). *Geophysical Journal International*, 167(3), 1220-1232. [https://doi.org/10.1111/j.1365-](https://doi.org/10.1111/j.1365-246X.2006.03083.x)
862 [246X.2006.03083.x](https://doi.org/10.1111/j.1365-246X.2006.03083.x)
- 863 Zhu, W., & Beroza, G. C. (2019). PhaseNet: a deep-neural-network-based seismic arrival-time picking method.
864 *Geophysical Journal International*, 216(1), 261-273. <https://doi.org/10.1093/gji/ggy423>
865